AIAA JOURNAL
Vol. 30, No. 5, May 1992

Locally Implicit Hybrid Algorithm for Steady and Unsteady Viscous Flows

C. J. Hwang* and J. L. Liu†
National Cheng Kung University, Taiwan 70101, Republic of China

A locally implicit hybrid finite volume algorithm on mixed type of triangular and quadrilateral meshes for the two-dimensional steady and unsteady viscous flows has been developed. The unsteady, full Navier-Stokes equations are solved in the Cartesian coordinate system. A new construction of a total-variation-diminishing formulation on triangles is used to obtain high-resolution results in the convective-dominated flow region. In the viscous-dominated part, a second- and fourth-order dissipative model on quadrilateral grids is employed to minimize the numerical dissipation. To investigate the accuracy and characteristics of the present total-variation-diminishing scheme, the nonlinear Burgers' equation and inviscid flows passing through channels with sinusoidal bump in steady subsonic and unsteady transonic regimes are solved. The evaluation of the locally implicit hybrid algorithm for steady viscous flow is performed by studying the shock/boundary-layer interaction and transonic flows around a NACA 0012 airfoil and turbine cascade. To confirm the reliability and accuracy of the present numerical algorithm using time-accurate calculations, the viscous flow for an oscillating flat plate is investigated. Satisfactory agreement between numerical results and exact solutions for the Stokes' second problem is obtained.

Introduction

RECENTLY, considerable efforts have been expended in developing reliable and efficient computational methods on unstructured meshes. Many algorithms utilize explicit time integration to steady-state solutions due to its simplicity and ease to implement.[1,2] In general, explicit methods are easy to program and vectorize and require only limited computer memory and no matrix inversions. However, the Courant-Friedrichs-Lewy (CFL) number condition limits the time step, especially for the solutions of the Navier-Stokes equations. On the other hand, several implicit schemes have been presented.[3,4] These schemes are not bounded by stability limitations, and the sparse matrix solver or point Gauss-Seidel approach with sweep pattern and renumbering techniques are used. For several explicit and implicit schemes on unstructured triangular meshes, the storage space, convergence rate, and CPU times have been investigated and described by Whitaker et al.[5] Besides explicit and fully implicit approaches, the semi-implicit[6] and locally implicit schemes[7] were developed on the structured quadrilateral meshes. In the present work, the time integration technique used in Ref. 7 is extended for solving the steady and unsteady viscous flows on mixed unstructured triangular and structured quadrilateral meshes. The renumbering of cells and matrix system solvers are not used.

Jameson and Mavriplis[1,8] developed an explicit finite volume algorithm for cell-centered and nodal schemes to solve the Euler equations. These schemes contain second- and fourth-order artificial dissipation terms on triangular meshes. In the structured quadrilateral grid system, Yee[9,10] has modified and generalized Harten's second-order total-variation-diminishing (TVD) scheme to explicit and implicit non-monotone upstream-centered schemes for conservation laws (MUSCL)-type approaches for steady-state as well as unsteady flow calculations. To remove the local restrictions of the TVD schemes at extreme points, Harten et al.[11] and Yang and Lombard[12] presented the essentially nonoscillatory (ENO) schemes that retain uniformly second-order accuracy throughout. The features of the TVD and ENO schemes are studied by Chang and Liou.[13] On unstructured meshes, Hwang and Liu[14] have constructed a symmetric TVD scheme on triangular cells. For the inviscid airfoil and channel flows, the scheme yields good results. In the present paper, the symmetric TVD scheme of Ref. 14 is further improved for obtaining higher order accuracy near extreme points. This scheme is successfully applied to solve the nonlinear Burgers' equation and steady subsonic and unsteady transonic inviscid flows passing through channels with sinusoidal bump.

In the application of TVD-type schemes to viscous flows, the question of whether the numerical dissipation terms (due to the TVD-type terms) have an adverse effect on the true viscosity terms in the boundary-layer regions is the topic of study.[10] For supersonic separated flows, Chamberlain[15] indicated that the use of a switching procedure that recognizes viscous and expansion regions and avoids excessive limiting (dissipation) might be useful for retaining the desirable properties of limiters without smearing out solution details in the regions of interest. To accurately simulate the viscous flows, a hybrid finite volume algorithm was developed in this work. In the convective-dominated part, an improved symmetric TVD scheme is used to obtain high-resolution results. In the viscous-dominated region, the second- and fourth-order dissipative model[7] is implemented to minimize the numerical dissipation. The evaluation of this hybrid finite volume algorithm on quadrilateral grids is performed by studying the shock/boundary-layer interaction problem.

Currently, flows around airfoils and cascade blades are usually investigated by using the conventional flow solvers, which are based on the structured quadrilateral meshes (C-mesh, O-mesh, H-mesh, etc.). In practice, the implementation of flow solvers on the structured grids is often highly constrained by complex geometry. Thus, it is very difficult to construct a single structured grid system for geometrically complex two- or three-dimensional bodies. To overcome these problems, unstructured meshes[1,2] or zonal approaches with the composite or overlaid grid systems (quadrilateral or triangular meshes)[16,17] have been developed. It is known that purely triangular meshes are, however, very inefficient in boundary layers for viscous flow where the flow gradients are strongly one dimensional. A better approach is to create a set of computationally efficient

Received Dec. 3, 1990; revision received May 1, 1991; accepted for publication May 19, 1991.

*Associate Professor, Institute of Aeronautics and Astronautics. Member AIAA.
†Graduate Student.

high aspect ratio quadrilateral cells in the boundary layer around the blade surfaces. Outside the structured mesh, an unstructured triangular mesh can be used. In this work, the C- or O-type quadrilateral mesh is placed on the airfoil or the blade surface to facilitate the one-dimensional stretched requirement for the efficient resolution of the viscous effects. Unstructured triangular meshes are constructed elsewhere. The Baldwin-Lomax turbulence model[18] is implemented easily on the structured quadrilateral grids. To demonstrate the accuracy and reliability of the present locally implicit hybrid algorithm on mixed triangular and quadrilateral meshes for the steady and unsteady viscous flows, the transonic turbulent flows for a NACA 0012 airfoil and turbine cascade and laminar flows for an oscillating flat plate, are investigated.

Governing Equations

The two-dimensional, unsteady Reynolds-averaged Navier-Stokes equations in dimensionless conservation-law form can be written in the Cartesian coordinate system

$$\frac{\partial U}{\partial t}+\frac{\partial E}{\partial x}+\frac{\partial G}{\partial y}=\frac{1}{Re}\left[\frac{\partial R}{\partial x}+\frac{\partial S}{\partial y}\right] \tag{1}$$

where

$$U=\begin{bmatrix}\rho\\ \rho u\\ \rho v\\ e\end{bmatrix},\quad E=\begin{bmatrix}\rho u\\ \rho u^2+P\\ \rho uv\\ (e+P)u\end{bmatrix},\quad G=\begin{bmatrix}\rho v\\ \rho uv\\ \rho v^2+P\\ (e+P)v\end{bmatrix}$$

$$R=\begin{bmatrix}0\\ \tau_{xx}\\ \tau_{xy}\\ r_4\end{bmatrix},\quad S=\begin{bmatrix}0\\ \tau_{xy}\\ \tau_{yy}\\ s_4\end{bmatrix}$$

$$\tau_{xx}=2\mu u_x+\lambda(u_x+v_y)$$

$$\tau_{yy}=2\mu v_y+\lambda(u_x+v_y)$$

$$\tau_{xy}=\mu(u_y+v_x)$$

$$r_4=u\tau_{xx}+v\tau_{xy}+\frac{1}{\gamma-1}\left(\frac{\mu_l}{Pr_l}+\frac{\mu_t}{Pr_t}\right)(a^2)_x$$

$$s_4=u\tau_{xy}+v\tau_{yy}+\frac{1}{\gamma-1}\left(\frac{\mu_l}{Pr_l}+\frac{\mu_t}{Pr_t}\right)(a^2)_y$$

$$\mu=\mu_l+\mu_t$$

In these equations, the subscripts l and t refer to laminar and turbulent flows, respectively. The variables ρ, u, v, e, and a represent the gas density, velocity components in the x and y directions, total energy per unit volume, and the speed of sound, respectively. The Reynolds number and Prandtl number are denoted as Re and Pr. The pressure P is obtained by the equation of state for perfect gas. The parameters μ and λ are the coefficients of viscosity, and λ is taken to be $-2/3\mu$. The molecular viscosity μ_l is determined by the Sutherland's law. The two-layer algebraic turbulence model of Baldwin and Lomax[18] is used to estimate the eddy viscosity μ_t, and the Reynolds heat flux terms are approximated by using the constant Prandtl number assumption.

Numerical Algorithm

Finite Volume Formulation on Triangular Meshes

The governing equations in Eq. (1) can be rewritten in the vector form as

$$\frac{\partial U}{\partial t}+\nabla\cdot(\boldsymbol{F}-\boldsymbol{D})=0 \tag{2}$$

where $\boldsymbol{F}$ and $\boldsymbol{D}$ represent the convective and viscous flux vectors, respectively. By integrating Eq. (2) over space and using the Gauss theorem, the integral form for a bounded domain Ω with a boundary $\partial\Omega$ is given as follows,

$$\frac{\partial}{\partial t}\int\int_{\Omega}U\,dA+\int_{\partial\Omega}(\boldsymbol{F}-\boldsymbol{D})\cdot d\boldsymbol{l}=0 \tag{3}$$

where $d\boldsymbol{l}=\boldsymbol{n}\,dl$, and $\boldsymbol{n}$ is the unit normal vector in the outward direction. The cell-centered finite volume formulation on a triangular cell i shown in Fig. 1 is expressed as

$$\frac{\partial}{\partial t}(U\,A)_i=-Q_i(U) \tag{4}$$

where

$$Q_i(U)=\sum_{k=1}^{3}(\boldsymbol{F}\cdot d\boldsymbol{l})_{ik}-\sum_{k=1}^{3}(\boldsymbol{D}\cdot d\boldsymbol{l})_{ik}$$

$$=Q_i^c(U)+Q_i^v(U)$$

Inviscid Flux Function $Q_i^c(U)$

The numerical inviscid flux function $Q_i^c(U)$ of Eq. (4) at each cell interface ik in the Cartesian coordinate system is expressed as[14]

$$\sum_{k=1}^{3}(\boldsymbol{F}\cdot d\boldsymbol{l})_{ik}=\frac{1}{2}\sum_{k=1}^{3}\{(\boldsymbol{F}_i+\boldsymbol{F}_k)\cdot d\boldsymbol{l}_{ik}-R_{ik}\Psi(\Lambda_{ik})[\Delta\alpha_{ik}-\Delta\bar{\alpha}_{ik}]\} \tag{5}$$

where the matrix R_{ik} is the eigenvector of the Jacobian matrix $[(\partial\boldsymbol{F}/\partial U)\cdot d\boldsymbol{l}]_{ik}$, and R_{ik}^{-1} is the inverse matrix of R_{ik}. The eigenvector matrix R_{ik} is evaluated by Roe's average on the interface between cell i and cell k. The matrix $\Delta\alpha_{ik}$ has the elements of $R_{ik}^{-1}(U_k-U_i)$, and Λ_{ik} is a diagonal matrix in which the diagonal terms are composed of eigenvalues of the Jacobian matrix $[(\partial\boldsymbol{F}/\partial U)\cdot d\boldsymbol{l}]_{ik}$. The function $\Psi(\Lambda_{ik})$ is an entropy correction and has the following form:

$$\Psi(\Lambda_{ik})=\begin{cases}|\Lambda_{ik}| & \text{if } |\Lambda_{ik}|\geq\epsilon_{ik}\\ \dfrac{(\Lambda_{ik}^2+\epsilon_{ik}^2)}{2\epsilon_{ik}} & \text{otherwise}\end{cases} \tag{6}$$

where

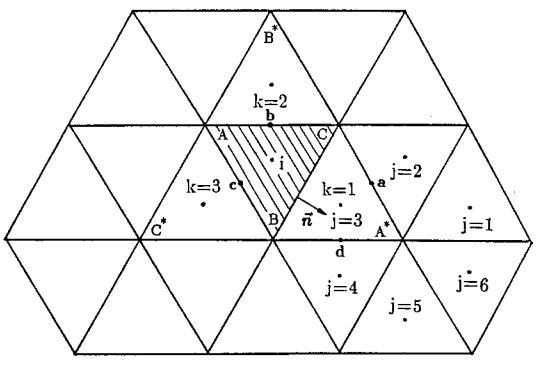

Fig. 1 Definitions of unstructured triangular mesh and auxiliary cells for the cell-centered TVD scheme.

$$\epsilon_{ik} = \epsilon[|\boldsymbol{V}\cdot d\boldsymbol{l}| + a|d\boldsymbol{l}|]_{ik} I$$

$$I = \text{diag}[1, 1, 1, 1]$$

and the ϵ is a small positive coefficient taken as 0.1.

The limiter function $\Delta\bar{\alpha}_{ik}$ is given by

$$\Delta\bar{\alpha}_{ik} = \text{minmod}(\Delta\alpha_{ik}, \Delta\alpha_{ik}^{+}, \Delta\alpha_{ik}^{-}) \tag{7}$$

where $\Delta\alpha_{ik}^{+} = R_{ik}^{-1}(U_{L^*} - U_{ik})$, $\Delta\alpha_{ik}^{-} = R_{ik}^{-1}(U_{ik} - U_L)$, and L is the index of A, B, or C. For example, $L = A$ for $k = 1$ is shown in Fig. 1. The use of a limiter function is to interpolate for higher order accuracy of the solution. In this paper, the interpolation is constructed by choosing the properties at cell centers (U_i and U_k) and nodal points (U_L and U_{L^*}). At the nodes, the properties are obtained by the area-weighting rule. For example, the quantity U_{A^*} (see Fig. 1) can be written as

$$U_{A^*} = \left(\sum_{j=1}^{6} U_j A_j\right) \Big/ \left(\sum_{j=1}^{6} A_j\right) \tag{8}$$

The main advantage of the TVD schemes is to produce high-resolution results around shock and contact discontinuities. It is well known that one of the drawbacks of high-order TVD schemes is that they reduce to first-order at points of extrema.[10] To compensate for this local drawback, an improvement for those extreme points is introduced in this paper. When the value of $\Delta\bar{\alpha}_{ik}$ in Eq. (7) is equal to zero, the expression of the limiter function is replaced by a new alternative form given as follows:

$$\Delta\bar{\alpha}_{ik} = \sigma_{ik}\,\text{sign}(\Delta\alpha_{ik})\,\min(|\Delta\alpha_{ik}|, |\Delta\alpha_{ik}^{+}|, |\Delta\alpha_{ik}^{-}|) \tag{9}$$

where

$$\sigma_{ik} = \bar{\sigma}_{ik} H(1 - 32\bar{\nu}_{ik})$$

$$\bar{\sigma}_{ik} = 1 - \frac{|\nabla U_i|}{(|U_i| + |U_k|)}$$

$$\nu_i = \frac{|\nabla^2 P_i|}{\sum_{k=1}^{3} (P_i + P_k)}$$

$$\bar{\nu}_{ik} = \max(\nu_i, \nu_k, \nu_{k1}, \nu_{k2}, \nu_{k3})$$

$$\nabla^2 P_i = \sum_{k=1}^{3} P_k - 3P_i$$

The subscripts $k1$, $k2$, and $k3$ represent the indices of three triangular cells that surround the cell k (see Fig. 1). The expressions of sign($\Delta\alpha_{ik}$) and H indicate the sign of the value $\Delta\alpha_{ik}$ and the symbol of the unit step function, respectively. By using Eq. (9), the oscillations near discontinuities ($\sigma_{ik} = 0$) are suppressed and a higher order accuracy is obtained around the extreme points. The function $\bar{\sigma}_{ik}$ depends on the normalized first-order gradient of conservation variables. Because the TVD sufficient conditions are satisfied, the scheme with improved form in Eq. (9) is still TVD for a one-dimensional model equation. Numerical experiments in this work have shown that the improved TVD scheme is robust and increases the accuracy of the numerical solutions.

Viscous Flux Function $Q_i^v(U)$

To evaluate the numerical viscous flux vector $\boldsymbol{D}$ at the cell interfaces, it is necesary to compute the shear stress and the heat conduction terms. A new treatment for the viscous flux on the unstructured triangular mesh is introduced. The first-order derivatives of the velocity components and the sound speed are calculated by constructing auxiliary cells and using Green's theorem for surface integration. For example, the discretized forms of u_x and u_y at interface $i1$ between cell i and cell 1 (see Fig. 1) are

$$(u_x)_{i1} = \frac{1}{(A_i + A_1)} \sum_{p=a}^{d} u_p \Delta y_p \tag{10}$$

$$(u_y)_{i1} = -\frac{1}{(A_i + A_1)} \sum_{p=a}^{d} u_p \Delta x_p \tag{11}$$

The summation over p refers to the four midpoints of the sides for the auxiliary cell A^*CAB. The properties at the points a, b, c, and d are obtained by arithmetical average of properties at each of the two neighboring cells. The viscous flux, which includes streamwise- and crosswise-like gradients of shear stress and heat conduction terms, is considered. Thus, the full Navier-Stokes equations are solved on the unstructured triangular mesh in the present work.

Hybrid Algorithm on Mixed Type of Triangular and Quadrilateral Meshes

By solving the full Navier-Stokes equations, a hybrid finite volume algorithm on a mixed type of quadrilateral and triangular meshes is developed to accurately simulate viscous flow phenomena. On the structured quadrilateral cells, the second- and fourth-order dissipative model[7] is applied to minimize the numerical dissipation in the boundary layer and/or wake regions. The numerical formulations presented by Swanson[19] and Reddy and Jacocks[7] are introduced. In the convective-dominated part of the flowfield, the improved symmetric TVD scheme on the unstructured triangular elements is used to obtain high-resolution results. Even though two different kinds of numerical formulations are employed on the two major parts (inviscid- and viscous-dominated regions), the viscous terms are retained for the entire flowfield to avoid the problem related to distinction between viscous shear layer and inviscid core flow. The algebraic turbulence model of Ref. 18 is implemented on the quadrilateral grids only.

Time Integration

A two-parameter family of a time integration scheme for Eq. (4) on each triangular cell i (see Fig. 1) can be written as

$$A_i\left(\frac{U^{n+1} - U^n}{\Delta t}\right)_i + \frac{\theta}{1+\beta} Q_i(U^{n+1}) = -\frac{1-\theta}{1+\beta} Q_i(U^n) + \frac{\beta}{1+\beta}\left(\frac{A}{\Delta t}\right)_i (U_i^n - U_i^{n-1}) \tag{12}$$

where $0 \le \theta \le 1$ and $-1/2 \le \beta \le 1/2$. This kind of time integration approach consists of implicit ($\theta \neq 0$) as well as explicit ($\theta = 0$) schemes. In the present steady-state flow calculations, the first-order accuracy in time is retained by choosing $\theta = 1$ and $\beta = 0$. For the unsteady computations, $\theta = 1$ and $\beta = 1/2$ are used and the scheme becomes second-order accurate in time. In the viscous terms, U^{n+1} is obtained by iteration for unsteady calculation; however, U^{n+1} is treated explicitly as U^n for steady-state computation. By using the Taylor series expansion for the temporal difference of inviscid flux terms, Eq. (12) is linearized and can be constructed in the delta form as follows,

$$L_i(\Delta U) = Res_i^n = Rinv_i + Rvis_i + \frac{\beta}{1+\beta}\left(\frac{A}{\Delta t}\right)_i (U_i^n - U_i^{n-1}) \tag{13}$$

where

$$L_i(\Delta U) = CI\Delta U_i + CK_1\Delta U_1 + CK_2\Delta U_2 + CK_3\Delta U_3$$

$$Rinv_i = -\frac{1}{1+\beta} Q_i^c(U^n)$$

$$Rvis_i = -\frac{1}{1+\beta}\{\theta Q_i^v[U^{(m+1)}] + (1-\theta)Q_i^v(U^n)\}$$

$$CI = \left(\frac{A}{\Delta t}\right)_i \mathrm{I} + \frac{\theta}{2(1+\beta)}\sum_{k=1}^{3} \times \left\{M_{ik} + R_{ik}\Psi(\Lambda_{ik})R_{ik}^{-1}\left(1 - \frac{\Delta\bar{\alpha}_{ik}}{\Delta\alpha_{ik}}\right)\right\}$$

$$CK_L = \frac{\theta}{2(1+\beta)}\left\{M_{iL} - R_{iL}\Psi(\Lambda_{iL})R_{iL}^{-1}\left(1 - \frac{\Delta\bar{\alpha}_{iL}}{\Delta\alpha_{iL}}\right)\right\}, \quad L = 1, 2, 3$$

$$M_{ik} = \left(\frac{\partial \boldsymbol{F}}{\partial U}\cdot d\boldsymbol{l}\right)_{ik}$$

Equation (13) is solved by a modified Gauss-Seidel approach. It is not required to renumber the triangular cells and assemble any global matrices. The calculation for a symmetric cycle of inner iterative corrections is performed by starting at the first element and sweeping to the latest element ($m = 1$) followed by an opposite sweep ($m = 2$). Thus, for each cell i, Eq. (13) is written as

$$C\,dU_i = Res_i^n - L_i(\Delta U) \tag{14}$$

$$\Delta U_i^{(m+1)} = \Delta U_i^{(m)} + w_{\text{in}}\,dU_i, \qquad m = 1, 2 \tag{15}$$

The matrix C is approximated as a diagonal matrix, which is derived from a modification to the coefficient matrix CI.

$$C = \left\{\left(\frac{A}{\Delta t}\right)_i\left[\left(1.0 + \frac{\theta}{2(1+\beta)}\,\mathrm{CFL}\right)\right]\right\}I \tag{16}$$

ΔU, shown on the right-hand side of Eq. (14), takes the latest available values from Eq. (15). When the unsteady viscous calculation is employed, the properties $U^{(m+1)}$ in term $Rvis_i$ [Eq. (13)] is updated according to the following equation:

$$U_i^{(m+1)} = U_i^n + \Delta U_i^{(m+1)}, \qquad m = 2 \tag{17}$$

One symmetric cycle of inner iterations is employed in each time step for steady-state flows, whereas several cycles are performed until a convergence state of $\Delta U_i^{(m+1)}$ is reached for unsteady flow calculations. At the end of a time step, the outer relaxation is introduced,

$$U_i^{n+1} = U_i^n + w_{\text{out}}\Delta U_i \tag{18}$$

The coefficients w_{in} and w_{out} in Eqs. (15) and (18) are inner and outer relaxation parameters, respectively, of the order 1.2 (over-relaxation), whereas w_{out} is chosen as 1.0 for unsteady flow computations.

Boundary Conditions and Mesh Generation

At the airfoil, blade, or wall surface, no-penetration and no-slip conditions are imposed for the inviscid and viscous flows, respectively, and the adiabatic wall condition is assumed. For the subsonic and transonic flows passing through channels with sinusoidal bump, one-dimensional characteristics are used to treat inlet and outlet conditions. For the supersonic flow over a flat plate, the freestream conditions are specified at inlet, and zero-order space extrapolation is applied on the exit plane. In the calculation of transonic airfoil flow, the upstream flow angle is imposed, and the entropy, tangential velocity component, and Riemann invariants are extrapolated from the freestream or interior points. For the cascade flow, the total pressure, total temperature, and flow angle are specified at the inlet; the velocity magnitude is obtained from the values of interior points. On the exit plane, the static pressure is prescribed; the density and velocity components are extrapolated from the adjacent interior cells. In addition, the periodicity condition for cascade flow is easily satisfied by considering points outside the calculation domain to have the same flow properties as points one pitch distant within the domain and then equating all flow properties at corresponding points on the periodic boundaries. The viscous flow for the oscillating plate is computed by imposing periodic conditions on the upstream and downstream boundaries. On the plate surface, the velocity profile is specified, and the zero order extrapolation is used on the top of the computational domain. In this work, the flow solver is coupled with a mesh generation procedure that is capable of creating structured quadrilateral and unstructured triangular cells. For the generation of a mixed type of meshes, the quadrilateral grids are created first and then the interface nodes are set as boundary points for the triangular elements. The quadrilateral meshes for C- and O-type grids are constructed by the use of Poisson's equation,[20] and the triangular meshes are generated based on the advancing front concept.[21]

Results and Discussion

The approach just described is applied to compute inviscid and viscous flows through different regimes (subsonic, transonic, and supersonic flows). To investigate the characteristics of the present solution algorithms (improved symmetric TVD and hybrid schemes), the second- and fourth-order dissipative models[7,22] and symmetric TVD formulations[9,14] are also included in the cell-centered finite volume discretization on the quadrilateral and/or triangular meshes. Comparing with the related analytical and experimental data, the present locally implicit hybrid algorithm is proved to be accurate and reliable for studying the viscous steady and unsteady flows.

Improved Symmetric Total-Variation-Diminishing Scheme

One-Dimensional Burgers' Equation

To understand the accuracy and features of the improved symmetric TVD scheme, a numerical solution of the nonlinear Burgers' equation with periodic boundary condition is considered,

$$\frac{\partial u}{\partial t} + \frac{1}{2}\frac{\partial u^2}{\partial x} = 0, \qquad u(x, 0) = \sin\pi x \tag{19}$$

where $0 \le x \le 2$. The exact solutions and numerical results of original and improved symmetric TVD schemes are plotted in Fig. 2. When the time is equal to 0.2, the profile is still smooth and the improved symmetric TVD scheme shows a better result near the two points of extrema. When the time is equal to 1.0, a shock is developed at $x = 1.0$ where a discontinuity velocity profile is distributed. As depicted in Fig. 2, the improved formulation demonstrates a significant increase in the solution accuracy around the shock. The main reason for the difference of numerical results is that the original symmetric TVD scheme automatically reduces to first-or-

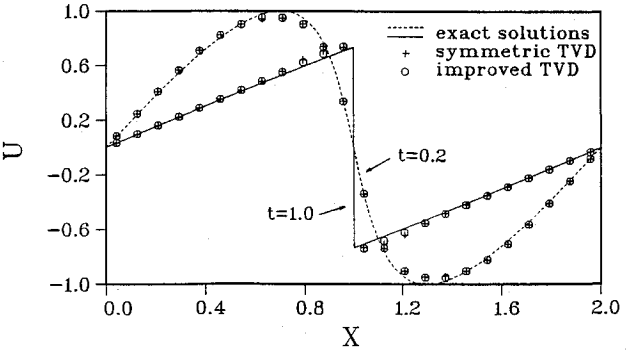

Fig. 2 Numerical results and exact solutions of Burgers' equation.

der accuracy whenever extreme points are encountered; however, the improved symmetric TVD scheme switches to an alternative correction term to compensate for this disadvantage.

Steady Subsonic Channel Flow

The order of accuracy of the present improved symmetric TVD scheme in two-dimensional flow is verified by studying subsonic flow ($M_\infty = 0.5$) passing through a channel. The channel consists of a length of 2.0, a width of 1.0, and a 10%-thick bump on the upper surface. The chord length of the bump is identical to the channel width, and the geometrical shape has a sinusoidal form.[23] Because the flow is subsonic throughout, no shock occurs and all losses for this computation are purely numerical errors of the schemes. In this study, rms of total pressure loss ($1.0 - P_t$) over the domain is used as a measure of these numerical losses. The mesh used here consists of unstructured triangular elements with approximately uniform grid space (ΔL). The results of the losses for varying grid space for four kinds of schemes are indicated in Fig. 3. The slope of each line is the scheme's order of accuracy. For the first-order TVD scheme, this value is 0.8. For the method with second- and fourth-order dissipation, the value of the slope is 1.8; it is around 1.71 for the original symmetric TVD scheme and 1.72 for the improved symmetric TVD scheme. The three schemes, therefore, are almost second-order accurate. From the previous discussion, it is apparent that the central difference formulation plus artificial dissipation model gives a better result than TVD schemes in the subsonic region, and the improved symmetric TVD scheme indicates less numerical error than the original TVD scheme.

Unsteady Transonic Channel Flow

To further understand the main difference between the original and improved symmetric TVD schemes, one unsteady transonic channel flow is studied. The geometry, flow conditions, and oscillating type of back pressure are the same as those of Bolcs et al.[23] On the fixed and uniform grid system with 2644 triangles, a CFL number of 5.0 is used. Choosing the steady-state solution (exit pressure $P_s = 0.7369$ and inlet Mach number $M_\infty = 0.675$) as the initial condition, the unsteadiness is introduced by varying the exit back pressure according to

$$P = P_s + P_{\text{amp}} \sin(\omega t) \tag{20}$$

where P_{amp} is the pressure amplitude equal to 0.12. In Eq. (20), $\omega/2$ is the nondimensional reduced frequency of the exit pressure fluctuation equal to 0.396. As displayed in Fig. 4, the upper and lower wall pressure distributions related to the oscillating back pressure during the second cycle of motion ($\omega t = 2\pi$ to $\omega t = 4\pi$) are selected for discussion. After finishing the first cycle calculation at $\omega t = (16/8)\pi$, the back pressure values repeat and begin to increase. Besides the shock, which already exists on the upper wall and becomes stronger, a compression shock occurs at the lower wall [$\omega t = (18/8)\pi$]. At $\omega t = (20/8)\pi$, the exit pressure has reached a maximum value, whereafter it starts to decrease. Because of the finite rate propagation of the pressure disturbance signals, the flow does not react instantaneously, and the shocks continue to move in the left direction [$\omega t = (22/8)\pi$]. Except for the results at $\omega t = (22/8)\pi$, the improved and original symmetric TVD schemes provide almost the same results. The shock at the lower wall is pushed farther into the subsonic region of the channel and becomes weaker because of the decrease in upstream flow velocity. At the same time, the upper wall shock is moved upstream, although the steady-state exit pressure is reached [$\omega t = (24/8)\pi$]. From the pressure distributions, the shock locations predicted by the two schemes are significantly different. At $\omega t = (25/8)\pi$, the flow is now subsonic throughout the channel, and the unsteady wave is still being propagated upstream. For this pressure train on the upper surface, the numerical accuracy of the original TVD scheme is reduced because several points of extrema are encountered. At $\omega t = (28/8)\pi$, the exit pressure has reached its minimum level. Whereafter, the pressure at the outlet begins to increase, and the upper wall shock steepens gradually. The second cycle (2π–4π) is finished when $\omega t = (32/8)\pi$ is reached. The pressure distributions obtained by using these two TVD schemes coincide together at this moment. The same flow structure of shock builds itself up as seen at $\omega t = (16/8)\pi$, whereafter the flow pattern will be repeated again. It is important to mention that a similar discussion of the physical behavior is also mentioned by Bolcs et al.[23]

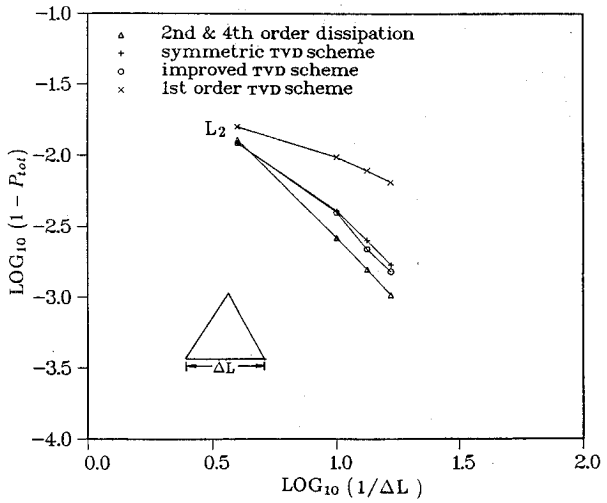

Fig. 3 Order of accuracy of the effects of schemes and grids on total pressure error for subsonic channel flow ($M_\infty = 0.5$).

Locally Implicit Hybrid Algorithm for Shock/Boundary-Layer Interaction Flow on Quadrilateral Mesh

The locally implicit hybrid algorithm for viscous flow is evaluated by studying the classical shock/boundary-layer interaction. The shock is sufficiently strong to cause flow separation in the boundary layer. The impinging shock is at an angle of 32.6 deg with respect to the freestream. The Reynolds number is 2.96×10^5, and it is based on freestream conditions and the length L from the leading edge of the plate to the shock impingement point. The freestream Mach number is 2.0, and it corresponds to the experiment of Hakkinen et al.[24] In this flow calculation, four kinds of schemes are employed on a quadrilateral mesh with 101×71 grid points. For the hybrid algorithm, the improved symmetric TVD scheme is used in the range $0.1 < y \leq 0.77$ and the second- and fourth-order dissipative model is applied in the region $0.0 \leq y \leq 0.1$. The present results are compared with the experimental data of Hakkinen et al.[24] as well as the computational results of Buelow[25] and Taylor et al.[26] For the skin-friction coefficient displayed in Fig. 5, the two TVD schemes give almost the same results, and the hybrid algorithm demonstrates the best agreement with the experimental data. The reason is that the TVD-type dissipation, which is implemented in the inviscid-dominated region, gives a good prediction of the boundary-layer edge properties and the second- and fourth-order dissipation is suitable for the subsonic boundary layer where the true viscosity effect is important.

Locally Implicit Hybrid Algorithm for Steady Viscous Flows on Mixed Type of Triangular and Quadrilateral Meshes

Transonic Airfoil Flow

To further demonstrate the capability of the locally implicit hybrid algorithm on the mixed type of grid system, the convective-dominated part is formulated by an improved symmetric TVD scheme on triangular meshes and the artificial dissipation model is introduced in the viscous-dominated region by using quadrilateral grids. In this computation, the turbulence model is implemented on the structured quadrilateral cells.

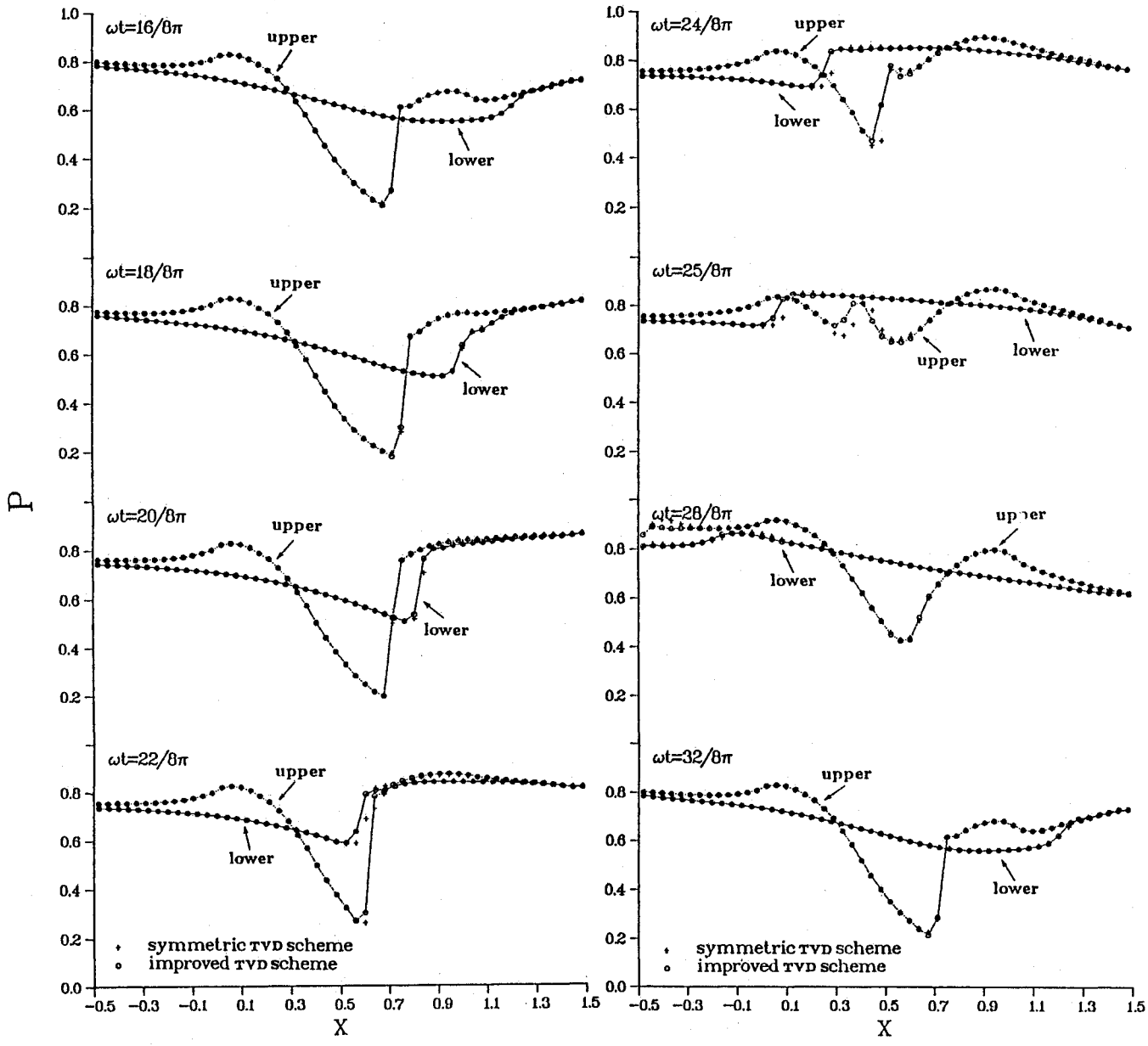

Fig. 4 Sequences of pressure distributions on upper and lower surfaces for transonic channel flow with time-varying back pressure.

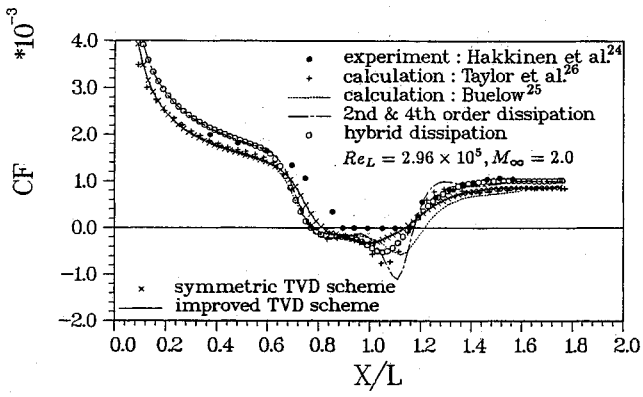

Fig. 5 Distributions of wall skin-friction coefficient for shock/boundary-layer interaction flow.

For the transonic turbulent flow over a NACA 0012 airfoil, the mesh is composed of C-type quadrilateral grids and unstructured triangular elements, which are displayed in Fig. 6a. The minimum cell distance between the first cell and the airfoil surface is 1.06×10^{-4} chord. The far-field boundaries of the computational domain are located at 10 chords, and 3122 triangular elements and 189 × 15 quadrilateral grid points are employed. In this airfoil flow ($M_\infty = 0.756$, $Re_\infty = 4.01 \times 10^6$) with zero angle of attack, the pressure distributions are presented in Fig. 6b. The hybrid algorithm and methods with the second- and fourth-order dissipative model exhibit similar solutions, whereas the results of the original and improved symmetric TVD schemes differ a little from the experimental data[27] near the extreme pressure point. Around the trailing edge, the two TVD schemes also yield inferior results.

Transonic Turbine Cascade Flow

The subsonic and transonic flows passing through an advanced turbine cascade have been extensively tested in four European wind tunnels for different exit flow conditions.[28] The flow with a Reynolds number of 8×10^5, based on the true chord length and the flow variables on the exit boundary, is

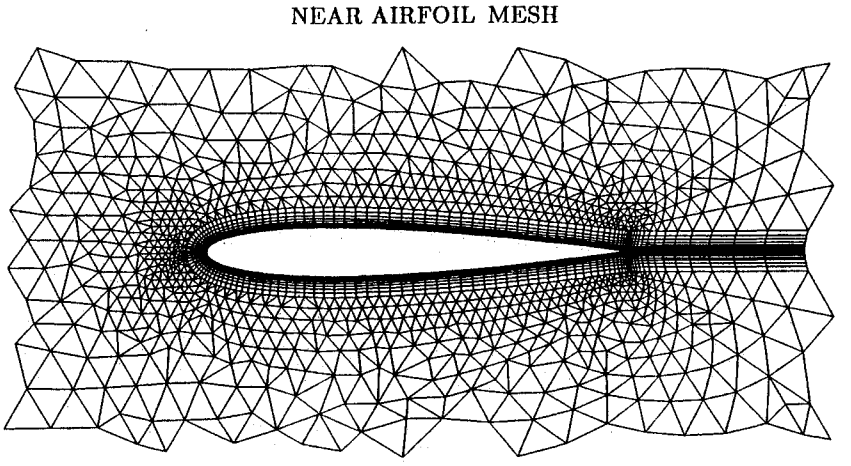

Fig. 6a Grid distribution for turbulent flow over a NACA 0012 airfoil.

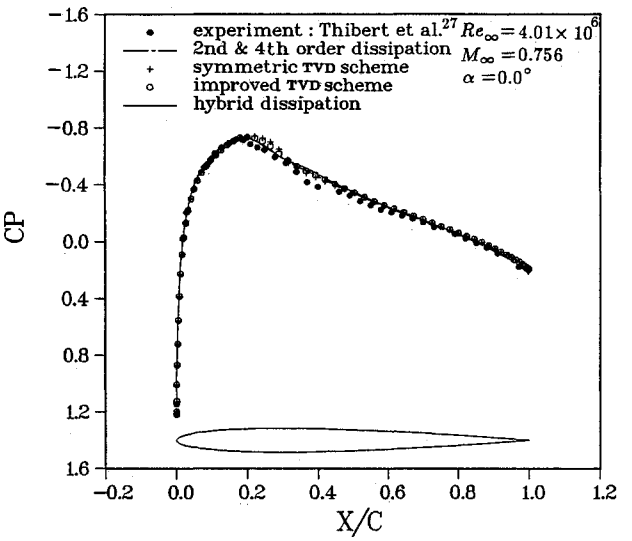

Fig. 6b Pressure distributions for turbulent flow over a NACA 0012 airfoil.

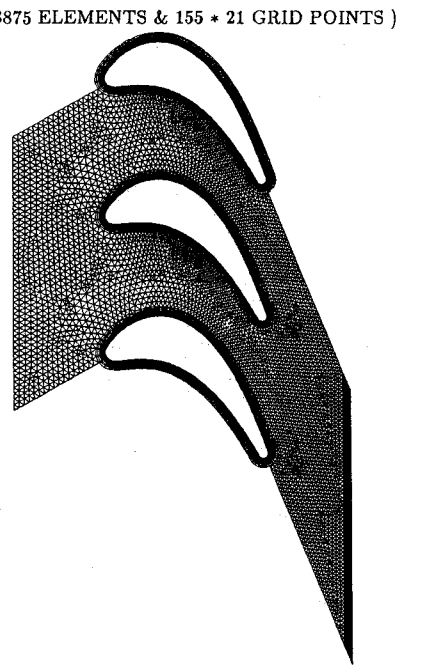

Fig. 7 Grid distribution for turbulent flow passing through the transonic turbine cascade.

investigated. The inlet angle and exit Mach number are equal to 30 deg and 0.966, respectively. In this paper, the calculation is carried out with the assumption of fully turbulent flow. As shown in Fig. 7, the flexible grid system, which contains the structured O-type quadrilateral grid around the blade and unstructured triangular elements elsewhere, is constructed. The minimum grid spacing between the first cell and the blade surface is 1.33×10^{-5} chord length. By using the locally implicit hybrid algorithm, the isentropic Mach number distribution and density contours are plotted in Fig. 8. Comparing with the experimental data,[28] the isentropic Mach number distribution on the blade surface is well predicted (see Fig. 8a). From the density contours (see Fig. 8b), the weak and strong shocks are formed on the suction side, and the wake is generated and interacts with the strong shock that occurs on the suction surface of the adjacent blade. Without using any other extra numerical treatment on the zonal boundaries, which is required by the conventional zonal approaches, Fig. 8b demonstrates that the smooth transition across the interface of triangular and quadrilateral cells is achieved.

Locally Implicit Hybrid Algorithm for Unsteady Viscous Flow on Mixed Type of Triangular and Quadrilateral Meshes

To evaluate the present locally implicit hybrid algorithm for unsteady viscous flow, Stokes' second problem[29] is studied. An infinitely long flat plate is surrounded by a stationary incompressible fluid and oscillates with the velocity $u(t) = u_0 \cos\omega t$, where u_0 and ω are the maximum amplitude and frequency of the oscillation, respectively. The exact solution, which represents the strongly damped oscillation, is given as follows,

$$\frac{u}{u_0} = \exp\left(-y\sqrt{\frac{\omega}{2\nu}}\right)\cos\left(\omega t - y\sqrt{\frac{\omega}{2\nu}}\right) \qquad (21)$$

In this computation, the analytical solution given in Eq. (21) is chosen as the initial condition on the quadrilateral grids near the flat plate (see Fig. 9), and the uniform stagnation properties are specified on the unstructured triangular elements. The Reynolds number and CFL number are equal to 1×10^4 and 3, respectively. As given in Fig. 10, the computed spatial distributions of x component of velocity at different time steps compare well with the exact solutions.

Conclusions

A locally implicit hybrid finite volume algorithm on mixed type of triangular and quadrilateral meshes for numerical integration of the unsteady, full Navier-Stokes equations has been

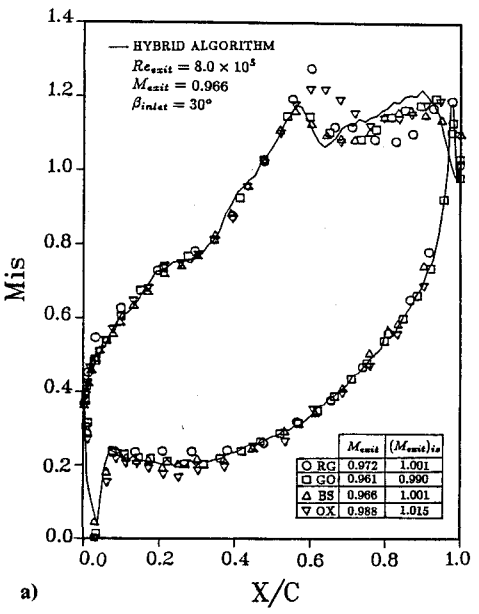

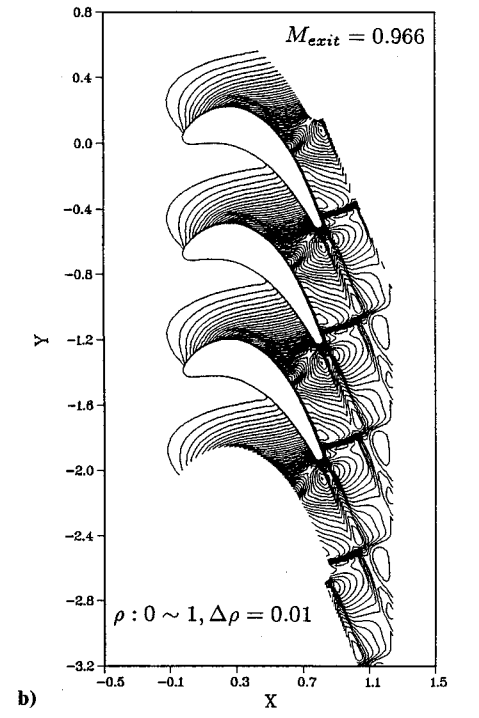

Fig. 8 Turbulent flow passing through the transonic turbine cascade: a) isentropic Mach number distributions; b) density contours.

developed in the Cartesian coordinate system. In this work, the convective-dominated part in the flowfield is formulated by an improved symmetric TVD scheme on triangles to obtain high-resolution results, and the second- and fourth-order dissipative model on quadrilateral grids is introduced in the viscous-dominated region to minimize the numerical dissipation. The accuracy of the improved symmetric TVD scheme, which is designed to compensate for the disadvantage of the original symmetric TVD scheme, is confirmed by the solutions of Burgers' equation and steady subsonic channel flow. For a transonic channel flow with a time-varying back pressure, the upper and lower wall pressure distributions are obtained as a function of time. The results provide a reasonable prediction of the flow phenomena and they also demonstrate the differences of the original and improved symmetric TVD schemes. To evaluate the locally implicit hybrid algorithm for viscous flow on quadrilateral grids, the classical problem of the shock/

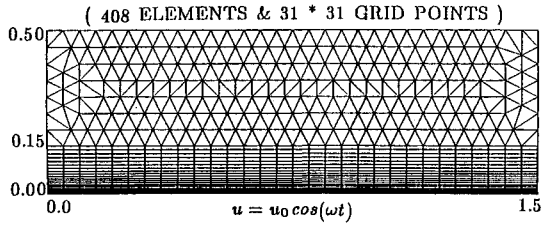

Fig. 9 Grid distribution for the viscous flow on the oscillating flat plate ($Re_L = 1.0 \times 10^4$).

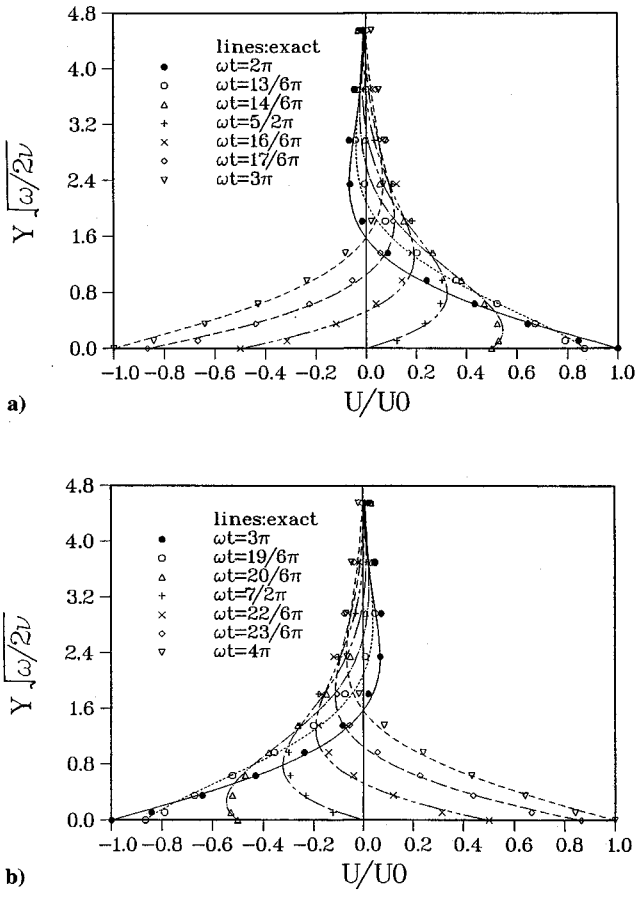

Fig. 10 X component velocity distributions for the viscous flow on the oscillating flat plate during a) 2π to 3π and b) 3π to 4π.

boundary-layer interaction is studied. Using mixed triangular and quadrilateral meshes, the transonic turbulent flows around a NACA 0012 airfoil and turbine cascade is studied. Comparing with the experimental data, the hybrid algorithm provides the most accurate results. For the time-accurate calculation, the reliability and accuracy of the present numerical algorithm on mixed meshes are confirmed by investigating the viscous flow over an oscillating flat plate (Stokes' second problem). It is concluded that the present locally implict hybrid algorithm, which is formulated on the flexible grid system with unstructured triangular and structured quadrilateral meshes, is accurate and robust.

References

[1]Mavriplis, D. J., "Accurate Multigrid Solution of the Euler Equations on Unstructured and Adaptive Meshes," *AIAA Journal*, Vol. 28, No. 2, 1990, pp. 213–221.

[2]McGrory, W. D., Walters, R. W., and Lohner, R., "A Three-Dimensional Space Marching Algorithm for the Solution of the Euler Equations on Unstructured Grids," AIAA Paper 90-0014, Jan. 1990.

[3]Venkatakrishnan, V., and Barth, T. J., "Application of Direct Solvers to Unstructured Meshes for the Euler and Navier-Stokes Equations Using Upwind Schemes," AIAA Paper 89-0364, Jan. 1989.

[4]Struijs, R., Vankeirsbilck, P., and Deconinck, H., "An Adaptive Grid Polygonal Finite Volume Method for the Compressible Flow Equations," AIAA Paper 89-1959, June 1989.

[5]Whitaker, D. L., Slack, D. C., and Walters, R. W., "Solution Algorithms for the Two-Dimensional Euler Equations on Unstructured Meshes," AIAA Paper 90-0697, Jan. 1990.

[6]Yee, H. C., and Shinn, J. L., "Semi-Implicit and Fully Implicit Shock-Capturing Methods for Hyperbolic Conservation Laws with Stiff Source Terms," AIAA Paper 87-1116, June 1987.

[7]Reddy, K. C., and Jacocks, J. L., "A Locally Implicit Scheme for the Euler Equations," AIAA Paper 87-1144, June 1987.

[8]Jameson, A., and Mavriplis, D. J., "Finite Volume Solution of the Two-Dimensional Euler Equations on a Regular Triangular Mesh," *AIAA Journal*, Vol. 24, No. 4, 1986, pp. 611–618.

[9]Yee, H. C., "Construction of Explicit and Implicit Symmetric TVD Schemes and Their Applications," *Journal of Computational Physics*, Vol. 68, No. 1, 1987, pp. 151–179.

[10]Yee, H. C., "A Class of High-Resolution Explicit and Implicit Shock-Capturing Methods," NASA TM-101088, Feb. 1989.

[11]Harten, A., Engquist, B., Osher, S., and Chakravarthy, S., "Uniformly High Order Accurate Essentially Non-Oscillatory Schemes, III," *Journal of Computational Physics*, Vol. 71, No. 2, 1987, pp. 231–303.

[12]Yang, J. Y., and Lombard, C. K., "Uniformly Second Order Accurate ENO Schemes for the Euler Equations of Gas Dynamics," AIAA Paper 87-1166, June 1987.

[13]Chang, S. H., and Liou, M. S., "A Comparison of ENO and TVD Schemes," AIAA Paper 88-3707, June 1988.

[14]Hwang, C. J., and Liu, J. L., "Locally Implicit Total-Variation-Diminishing Schemes on Unstructured Triangular Meshes," *AIAA Journal*, Vol. 29, No. 10, 1991, pp. 1619–1626.

[15]Chamberlain, R. R., "Influence of Flux Limiting on the Calculation of Supersonic Separated Flows Using Roe's Scheme," AIAA Paper 90-0588, Jan. 1990.

[16]Nakahashi, K., Nozaki, O., Kikuchi, K., and Tamura, A., "Navier-Stokes Computations of Two- and Three-Dimensional Cascade Flowfields," *Journal of Propulsion and Power*, Vol. 5, No. 3, 1989, pp. 320–326.

[17]Holmes, D. G., and Connell, S. D., "Solution of the 2D Navier-Stokes Equations on Unstructured Adaptive Grids," AIAA Paper 89-1932, June 1989.

[18]Baldwin, B. S., and Lomax, H., "Thin Layer Approximation and Algebraic Model for Separated Turbulent Flows," AIAA Paper 78-257, Jan. 1978.

[19]Swanson, R. C., "A Multistage Time-Stepping Scheme for the Navier-Stokes Equations," AIAA Paper 85-0035, Jan. 1985.

[20]Sorenson, R. L., "A Computer Program to Generate Two-Dimensional Grids About Airfoils and Other Shapes by the Use of Poisson's Equations," NASA TM 81198, May 1980.

[21]Lo, S. H., "A New Mesh Generation Scheme for Arbitrary Planar Domains," *International Journal for Numerical Methods in Engineering*, Vol. 21, No. 8, 1985, pp. 1403–1426.

[22]Hwang, C. J., and Liu, J. L., "Inviscid and Viscous Solutions for Airfoil/Cascade Flows Using a Locally Implicit Algorithm on Adaptive Meshes," Journal of Turbomachinery, Vol. 113, No. 4, 1991, pp. 553–560.

[23]Bolcs, A., Fransson, T. H., and Platzer, M. F., "Numerical Simulation of Inviscid Transonic Flow Through Nozzles with Fluctuating Back Pressure," *Journal of Turbomachinery*, Vol. 111, No. 2, 1989, pp. 169–180.

[24]Hakkinen, R. J., Greber, I., Trilling, L., and Abarbanel, S. S., "The Interaction of an Oblique Shock Wave with a Laminar Boundary Layer," NASA Memo 2-18-59W, March 1959.

[25]Buelow, P. E., "Comparison of TVD Schemes Applied to the Navier-Stokes Equations," AIAA Paper 89-0847, Jan. 1989.

[26]Taylor, A. C., III, Ng, W. F., and Walters, R. W., "An Improved Upwind Finite Volume Relaxation Method for High Speed Viscous Flow," AIAA Paper 89-0549, Jan. 1989.

[27]Thibert, J. J., Granjacques, M., and Ohman, L. H., "Experimental Data Base for Computer Program Assessment," NACA 0012 Airfoil, AGARD Advisory Rept. 138, May 1979, pp. A1–9.

[28]Kiock, R., Lehthaus, F., Baines, N. C., and Sieverding, C. H., "The Transonic Flow Through a Plane Turbine Cascade as Measured in Four European Wind Tunnels," *Journal of Engineering for Gas Turbines and Power*, Vol. 108, No. 2, 1986, pp. 277–284.

[29]White, F. M., *Viscous Fluid Flow*, McGraw-Hill, New York, 1974, pp. 148–149.